

Rates of Short-GRB afterglows in association with Binary Neutron Star mergers

M. Saleem^{1,*}, Archana Pai², Kuntal Misra³, L. Resmi⁴, and K. G. Arun^{5,6}

¹Indian Institute of Science Education and Research Thiruvananthapuram, CET Campus, Trivandrum 659016.

²Department of Physics, Indian Institute of Technology Bombay, Powai, Mumbai 400076.

³Aryabhata Research Institute of Observational Sciences, Nainital.

⁴Indian Institute of Space Science and Technology, Trivandrum.

⁵Chennai Mathematical Institute, Siruseri, 603103 Tamilnadu.

⁶Institute for Gravitation and the Cosmos, Pennsylvania State University, State College, PA 16802.

Accepted XXX. Received YYY; in original form ZZZ

ABSTRACT

Assuming all binary Neutron Star mergers produce Short Gamma Ray Bursts (SGRBs), we combine the merger rates of binary Neutron Stars (BNS) from population synthesis studies, the sensitivities of advanced Gravitational Wave (GW) interferometer networks, and of the electromagnetic (EM) facilities in various wave bands, to compute the detection rate of associated afterglows in these bands. Using the inclination angle measured from GWs as a proxy for the viewing angle and assuming a uniform distribution of jet opening angle between 3 to 30 degrees, we generate light curves of the counterparts using the open access afterglow hydrodynamics package BoxFit for X-ray, Optical and Radio bands. For different EM detectors we obtain the fraction of EM counterparts detectable in these three bands by imposing appropriate detection thresholds. In association with BNS mergers detected by five (three) detector network of advanced GW interferometers, assuming a BNS merger rate of $0.6 - 774 \text{ Gpc}^{-3} \text{ yr}^{-1}$ (Dominik et al. 2012), we find the afterglow detection rates (per year) to be $0.04 - 53$ ($0.02 - 27$), $0.03 - 36$ ($0.01 - 19$) and $0.04 - 47$ ($0.02 - 25$) in the X-ray, optical and radio bands respectively. Our rates represent maximum possible detections for the given BNS rate since we ignore effects of cadence and field of view in EM follow up observations.

Key words: gravitational waves – gamma ray bursts

1 INTRODUCTION

The observations of gravitational waves from compact binary merger events during the observational runs of the advanced LIGO detectors (LIGO-Hanford (H) and LIGO-Livingston (L)) and Virgo (V) detector have firmly established the era of gravitational wave (GW) astronomy (Abbott et al. 2016a,b, 2017a,b,c,d). The Japanese detector KAGRA (K) (Aso et al. 2013) is under construction and the approved LIGO-India (I) (Iyer et al. 2011) detector is expected to come up within a decade. With more number of detectors added, the global interferometric detector network will probe the distant Universe in GWs. Binary Black Hole (BBH), Binary Neutron Star (BNS) and Neutron Star-Black Hole (NSBH) mergers are among the prime targets of GW detectors. So far, 13 confirmed BNS systems are known (Tauris et al. 2017). NSBH systems have not yet been observed

in the electromagnetic (EM) window and hence the existence of these systems is an open puzzle. However, various binary formation channels predict their existence and there are population synthesis models which predict the rates (see for example Dominik et al. 2012).

The short gamma ray bursts (SGRBs) with T_{90} duration (time over which 90% of the total observed energy is emitted) less than 2 sec are short intense flashes of gamma rays releasing $\sim 10^{50}$ ergs of energy (see Berger 2014 for a review). BNS and NSBH mergers (collectively called as *NS mergers*) are believed to be the plausible progenitors of SGRBs (Narayan et al. 1992). A few hundreds of SGRBs are detected by all sky scanning γ -ray instruments. Recently, the observations of a SGRB (GRB170817A) in spatial and temporal coincidence with a GW observation from a BNS merger (GW170817) have given strong direct evidence for the NS-merger progenitor hypothesis (Abbott et al. 2017d,e,f). The era of multi-messenger astronomy will tremendously improve our understanding of the physical

* E-mail: saleemc87@iisertvm.ac.in

mechanisms of SGRB formation (Arun et al. 2014; Bartos et al. 2013; Granot et al. 2017).

GRBs are believed to be produced from relativistic jets of half opening angles of the order of a few degrees but due to strong relativistic beaming, the chances of detecting the prompt emission decreases if the observer's line of sight is not oriented to within the cone of the jet. The long wavelength counterparts of SGRBs known as the "afterglows" are potential EM counterparts of the GW signal. The nature of X-ray and radio counterparts of the recent joint event GW170817+GRB170817A was consistent to be as powered from a GRB jet pointed away from our line of sight (Abbott et al. 2017f; Troja et al. 2017; Alexander et al. 2017; Kim et al. 2017). Further, the observation of the optical/UV/NIR counterparts were indicative of the importance of kilonovae emission as EM counterparts of BNS merger events (Smartt et al. 2017; Arcavi et al. 2017; Pian et al. 2017). There are ongoing efforts for rapid EM follow up of the observed GW events in the EM window (GW-triggered EM follow-up) (Singer et al. 2014; Kasliwal & Nissanke 2014). With increasing number of GW detectors, we expect the sky error to reduce to as small as a few square degrees (Fairhurst 2011; Klimentenko et al. 2011; Tagoshi et al. 2014).

Coincident GW-SGRB detections have been addressed in literature in numerous contexts (Bartos et al. 2013; Siellez et al. 2013; Regimbau et al. 2015; Clark et al. 2015). Some of the previous studies focus on the scenario of joint detectability of GW transient and SGRBs/afterglows. For example, Metzger & Berger (2012) addresses the detectability issues of the EM-counterparts of the GW-detected NS mergers. Recently, Lazzati et al. (2016) explored the detectability of various EM components including prompt emission and afterglow in different EM bands. However, the authors fixed intrinsic GRB parameters and distance (200 Mpc) but studied the EM counterparts for different viewing angles. In Ghirlanda et al. (2016), authors estimate the rate of coincident SGRB-GW detections from the adLIGO BNS/NSBH detection volumes using luminosity distribution function and a redshift distribution of SGRBs. In Patricelli et al. (2016) the authors investigated the detectability of prompt emission and afterglow observed with *Fermi* in coincidence with BNS sources simulated as per population synthesis predictions. They considered three different values of θ_j (0.3, 10, and 30 deg) in their simulations. Feng et al. (2014) did a rather rigorous study to compute the detectability of late time radio afterglows in low radio frequencies (10 – 1800 MHz), relevant for the Square Kilometer Array (SKA) and its precursors, assuming SGRB rate to be the same as the BNS merger rate obtained in Abadie et al. (2010). They used *BoxFit*, a numerical hydrodynamic broad-band afterglow evolution code, to simulate afterglow light-curve and estimated the rates of radio afterglows (Van Eerten et al. 2012).

In this work, we estimate the rates of afterglow detections in various bands, associated with BNS mergers detected by advanced multi-detector ground based GW detectors. We consider *Swift* X-ray Telescope (XRT), the Large Synoptic Survey Telescope (LSST) and the Jansky Very Large Array (JVLA) for detections in X-ray, optical and radio bands respectively (optical afterglow detections with future wide-field instrument *LSST* is compared with the existing wide-field instruments *Pan-STARR1* and *DECam*).

We only consider the afterglow forward shock emission and calculate the light curves at 1 keV for X-ray, 4.5×10^{14} Hz for optical and 15 GHz for radio band using *BoxFit*. We carry out simulations to obtain a synthetic catalogue of mergers of BNS detected with 3- and 5-detector networks. As EM counterparts to the synthetic BNS detections, we simulate associated SGRB afterglow light curves, with luminosity distance and the inclination angle of the binary with respect to (w.r.t) the detector being used as proxies for their association. Apart from distance and inclination, we distribute other SGRB/afterglow parameters within their uncertainty regions obtained from the current observations as well as theoretical understanding of the SGRBs. We explore the afterglow parameter space rigorously and estimate the joint GW and SGRB afterglow rates for different distributions of the afterglow parameters.

Our study is based on several assumptions which are listed below:

- (i) BNS merger sources are uniformly distributed in volume in the universe with a density as predicted by population synthesis models in Dominik et al. (2012). Here, we ignore the effects of redshift since the detectable BNS sources are distributed in a closer volume (typically up to 750 Mpc [See Fig. 1] in which the redshift effects can be safely ignored.
- (ii) We consider all BNS systems to be non-spinning and made up of component masses of $1.4M_{\odot}$ each.
- (iii) We consider that all the BNS sources are observed by the LHV network and LHVKI detector network with each of them having noise PSD equal to the advanced LIGO designed sensitivity noise.
- (iv) We assume that all BNS mergers produce SGRB jets with an associated long wavelength afterglow in X-ray, optical and radio bands.
- (v) The calculations are for a uniform top-hat jet model, considered in the *BoxFit* code. It is possible that the jet structure could be different.
- (vi) While generating the light curves using *BoxFit* code, no correction for extinction (Galactic+host) has been made.
- (vii) We also ignore the limitations caused by the field of view (FOV) of EM counterpart follow-up instruments and the cadence of follow-up programs. In our work we consider that the follow-up observations have a minimum latency of 5 hours in current scenario.

The rest of this paper is organized as follows. In Section. 2 we introduce our method of rate estimation. In Section. 3, we describe our simulated BNS source population and their GW-detectability with a typical 3 detector network LHV and 5-detector network LHVKI. In Section. 4, we simulate afterglows as EM counterparts to the GW detected BNS sources and estimate their detectability with specific X-ray, optical and radio instruments. In Section. 5, we combine our findings and assumptions from previous sections and obtain the rates of various coincident joint GW and EM detection scenarios. Finally in Section. 7, we summarize our work and in Section. 6, we discuss the caveats and future prospects.

2 METHOD FOR RATE ESTIMATION

We use the below expression to calculate the detection rates $\mathbf{R}_{\text{AG,BNS}}$ of the SGRB afterglows in association with the

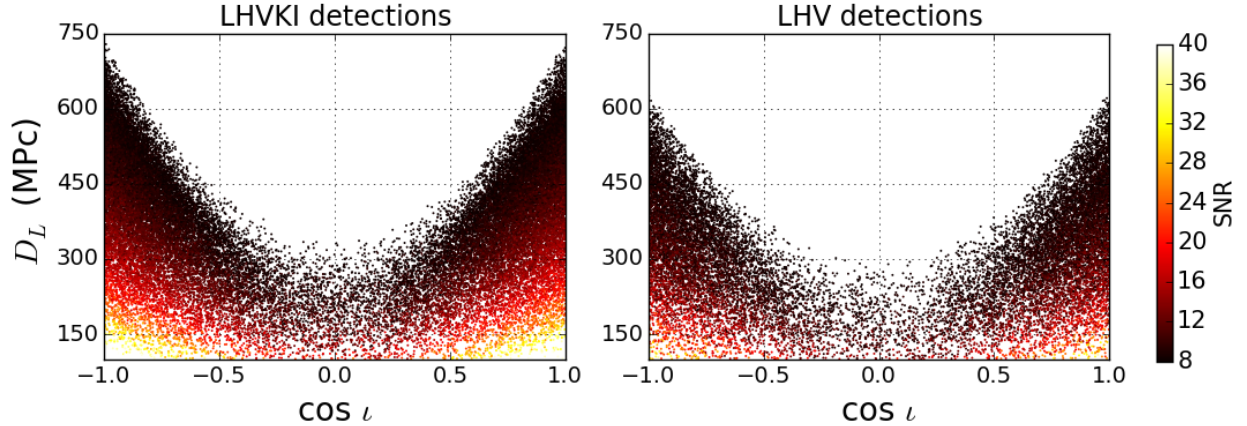


Figure 1. Distance-inclination ($D_L - \cos \iota$) scatter plots of the simulated non-spinning BNS sources detected at LHVKI (left) and LHV (right) networks with a detection criterion of minimum network SNR of 8. Face-on sources ($\cos \iota \rightarrow \pm 1$) are detected upto much larger distances than edge-on sources ($\cos \iota \rightarrow 0$) whose detections are possible only from nearby distances

GW-detected BNS merger events (ie, number of joint GW-afterglow detections per year),

$$\mathbf{R}_{\text{AG,BNS}} = \mathbf{r}_{\text{BNS}} \times \mathbf{V}_{\text{det}} \times \mathbf{f}_{\text{GWdet}} \times \mathbf{f}_{\text{AGdet}}, \quad (1)$$

where, each quantity introduced in the right hand side of Eq. 1 is described below.

- \mathbf{r}_{BNS} is the intrinsic BNS merger rate given in units of $\text{Gpc}^{-3}\text{yr}^{-1}$. In our case, we use the rates calculated by Dominik et al. (2012) based on population synthesis models which estimates the BNS merger rates to be $0.6 - 774 \text{Gpc}^{-3}\text{yr}^{-1}$
- \mathbf{V}_{det} is the detection volume of the GW detector network defined as the volume of a sphere centered at earth and extending up to the farthest source detectable by the given GW detector network (distance to which is referred to as horizon of the detector). For 3- and 5- detector networks, we compute this quantity in Section 3.
- $\mathbf{f}_{\text{GWdet}}$ is the detection fraction for a given GW detector network, defined as the fraction of BNS mergers detected from a source population which is uniformly distributed within the detection volume \mathbf{V}_{det} defined above. Please note that different detector networks have different sky coverage and hence the detection fraction will also vary for them. For LHV and LHVKI detectors, we compute $\mathbf{f}_{\text{GWdet}}$ in Section 3.
- $\mathbf{f}_{\text{AGdet}}$ is the detection fraction of the afterglow components, defined as the fraction of BNS-detected sources which has detectable afterglow by EM instruments. With simulated afterglow light-curves, we compute this quantity for different afterglow components in Section 4.

3 SIMULATED BNS SOURCES AND THEIR GW-DETECTABILITY

In this section, we estimate and compare the GW-detection volumes of 3- and 5 detector networks different detector networks and we also quantify the BNS detectability of each network within the detection volume. We consider a 3-detector network **LHV** which includes LIGO-Hanford(H), LIGO-Livingstone(L) and Virgo(V), and a 5-detector network **LHVKI** by adding the two upcoming detectors Kagra(K) and LIGO-India(I).

Table 1. Detection volume and detection fraction in the detection volume for different networks of GW detectors

Network	Horizon	$\mathbf{V}_{\text{det}}(\text{Gpc}^3)$	$\mathbf{f}_{\text{GWdet}}$
HLV	630Mpc	1.05	0.133 ± 0.003
HLVKI	730Mpc	1.63	0.181 ± 0.001

We simulated 3×10^5 non-spinning BNS sources with component masses $1.4M_{\odot}$ each, uniformly distributed in co-moving volume between 100-740Mpc. For each source, we simulated GW signal using the analytical 3.5 order post-Newtonian waveform (Blanchet 2006; Blanchet et al. 2004, 1995) and computed the network signal to noise ratio(SNR), defined as the quadrature sum of the SNRs in the individual detectors (Pai et al. 2001). With a minimum network SNR of 8 as the detection criterion, we recover 51834 sources with LHVKI and 24747 sources with LHV networks. The farthest source detected with LHVKI is at ~ 730 Mpc and for LHV, at ~ 630 Mpc which are defined as the horizon distances of each network and which in turn, can be used to compute the detection volumes of the networks as described in Section. 2. The detection fraction $\mathbf{f}_{\text{GWdet}}$ is the fraction of detected sources normalized w.r.t the total number of sources within the detection volume. In other words, detection fraction is obtained as the ratio of number of detected sources to the total number of sources within the detection volume. Note that all the sources within the detection volume are not detected because of the directional sensitivity of GW detectors. We have listed the detection volumes and detection fractions for LHVKI and LHV networks in Table. 3.

Figure. 1 shows the scattered plot of distance(D_L) and inclination angles (ι) of the detected BNS sources. Inclination angle ι is the angle between observer's line of sight and the axis of binary orbital plane. Left panel shows the $D_L - \cos \iota$ scatter plot for the sources detected by the LHVKI network and the right panel shows the same for LHV network with the color bar showing the SNR. For the actual simulated population which are uniformly distributed in volume, distance follows $P(D_L) \propto D_L^2$. However, due to the antenna

pattern functions, the GW detector networks have different sensitivities at different directions and hence the distant sources will be detectable only if they are located at highly sensitive directions. In other words, there will be a drop in average SNR for distances close to horizon which results in lesser number of detectable sources at larger distances (Schutz 2011).

In the simulated population, inclination ι of the binary is distributed such that $\cos \iota$ is uniform between -1 and 1, (ie, $P(\cos \iota) \propto \mathcal{U}(-1, 1)$ which translates as $P(\iota) \propto \sin \iota$). However, as seen in Figure. 1, the inclination distribution of detected sources is biased towards face-on sources ($\cos \iota \rightarrow \pm 1$) such that they are detectable to much larger distances than the edge-on sources ($\cos \iota \rightarrow 0$). Also, the color in Figure. 1 shows the SNR distribution of detected sources at two networks.

4 SIMULATED AFTERGLOWS AND THEIR DETECTABILITY

In this section, we describe our afterglow simulations associated with the 50,000 GW-detected BNS mergers shown in Figure.1. We have generated afterglow light-curves in radio, optical and X-ray bands using the open access hydrodynamic simulation package BoxFit (Van Eerten et al. 2012).

4.1 Associating GWs from BNS mergers with SGRB afterglows

The extrinsic afterglow parameters such as distance, inclination, sky location etc can be used to confirm the association between SGRB afterglow observations and binary neutron star mergers detected using GWs. Inclination ι of the binary in the GW literature is same as observer's viewing angle (θ_v) in the GRB literature, which is defined as the angle between the axis of the jet and the observers line of sight. Here one is implicitly assuming that the GRB jet is launched along the rotation axis of the black hole that is formed by the merger of the two neutron stars within the standard fireball paradigm. In our case, we use distance D_L and inclination ι (or viewing angle θ_v) as relevant GW inputs for simulating its EM counterparts (afterglow for here). Or in other words, using $D_L - \iota$ pair as a bridge, we associate a given GW-detected BNS merger and a SGRB afterglow to a single physical origin.

The association would be further strengthened if more parameters can be identified in common for the GW signal and the SGRB afterglow. The recent works Giacomazzo et al. (2012), Foucart (2012), Kawaguchi et al. (2016), Dietrich & Ujevic (2017) derive the disk mass M_{disk} and ejecta mass M_{ej} from the intrinsic parameters of progenitor binary such as component masses, spins and the equation of state parameter which are all obtained from GW observations. Such burst properties may be further used to derive the isotropic energy E_{iso} of the source. Salafia et al. (2017) considered a similar approach for estimating the detectability of EM counterparts of GW detected binaries and Coughlin et al. (2017) used the same for exploring the properties of kilonovae lightcurves. However, given the large uncertainties associated with the estimates of E_{iso} in this method, we have not employed this in the present paper.

Table 2. Components of afterglow parameter space along with their ranges and distributions. Prior range and distribution for the $D_L - \iota$ combination is obtained from GW-detection criteria. Remaining parameters are intrinsic to the afterglow generating mechanism and their prior ranges are taken as inferred from current observations. We have considered two populations of SGRB sources, namely population-1 and population-2, which differ in the distributions of E_{iso} , n and ϵ_B parameters. D_L and ι are directly chosen from the GW-detected population. \mathcal{U} denotes uniform distribution

Parameter	Range	Population-1	Population-2
D_L	–	GW prior	GW prior
θ_v	–	GW prior	GW prior
θ_j	(3°, 30°)	$P(\theta_j) \propto \mathcal{U}$	$P(\theta_j) \propto \mathcal{U}$
E_{iso} (erg)	$10^{49} - 10^{52}$	$P(\log E_{\text{iso}}) \propto \mathcal{U}$	$P(E_{\text{iso}}) \propto \mathcal{U}$
n (cm^{-3})	0.0001-0.1	$P(\log n) \propto \mathcal{U}$	$P(n) \propto \mathcal{U}$
ϵ_B	0.01 - 0.1	$P(\log \epsilon_B) \propto \mathcal{U}$	$P(\epsilon_B) \propto \mathcal{U}$
ϵ_E	0.1	fixed	fixed
p	2.5	fixed	fixed

4.2 Afterglow parameter space and lightcurves

Apart from extrinsic parameters D_L and θ_v which are obtained from GW detections (it is also possible to considerably refine D_L through spectroscopy of the optical host-galaxy, if detected), afterglow light curves depend on six intrinsic physical parameters of the emitting plasma. These are the isotropic equivalent kinetic energy E_{iso} carried by the jet, initial half opening angle of the jet θ_j , number density n of the circumburst medium (assumed to be homogeneous), fraction ϵ_B and ϵ_E of the shock thermal energy converted to downstream magnetic field and non-thermal electrons respectively, and power-law index p of energy-spectrum of the radiating electrons.

We have simulated 50,000 GRB afterglow lightcurves within the 8-dimensional afterglow parameter space described above. See Table-4.2 for the ranges and distribution of each parameters. In a companion paper (M. Saleem 2017), we describe in detail the justifications for choosing the ranges. The two populations considered differ only in the distribution of E_{iso} , n , and ϵ_B . We consider uniform (population-2) and logarithmic (population-1) distributions for these parameters as two extreme examples.

Since GW-detected θ_v distribution is allowed to have values anywhere between 0-180 (though it follows the distribution shown in Fig.1), and θ_j is only between 3-30, there are several sources for which $\theta_v > \theta_j$ (outside-jet). For our population, roughly 85% of the sources are outside-jet. This means that for a large fraction of the GW-detected sources, the probability of observing prompt emission is feeble. So afterglows become the most interesting EM counterparts to NS mergers.

4.3 EM facilities and detections

In this section, we detail the available/future EM facilities for afterglow detections along with the detection criterion used for this work. The representative instruments considered for X-ray, optical and radio observations are *Swift*-XRT, LSST and JVLA respectively. See Table. 3 the representative frequencies and threshold fluxes we used to calculate

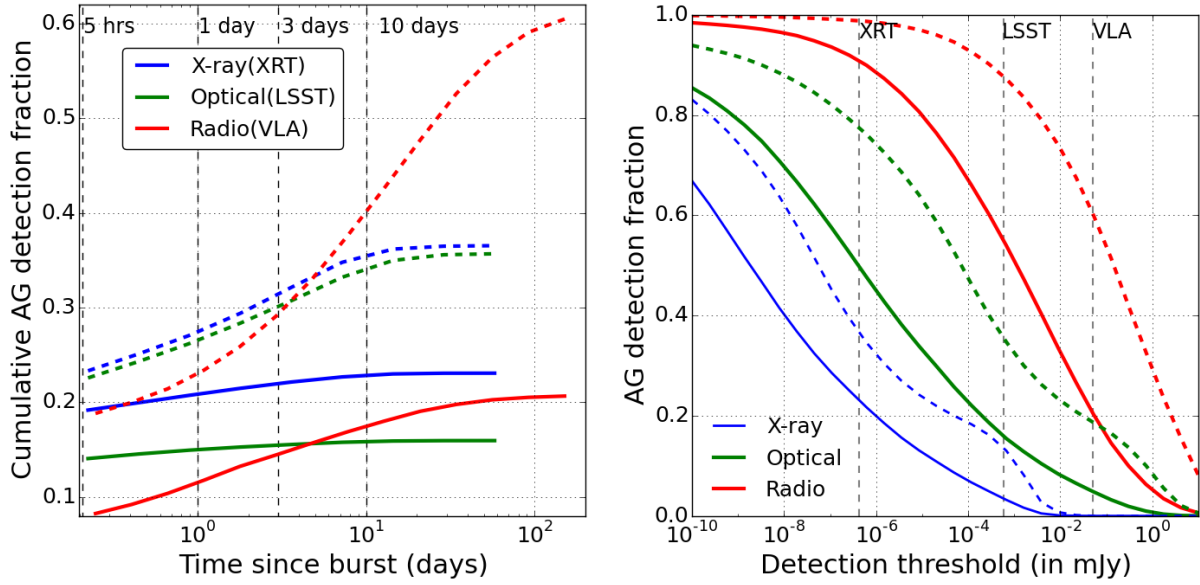


Figure 2. [Left] Cumulative afterglow detection fraction vs time since burst for population-1(solid lines) and population-2(dashed lines). Figure shows how the detection fraction of different afterglow components grow as a function of the time after the burst for a GW-detected BNS source population with 5-detector network LHVKI. [Right] Detection fraction vs detection threshold. Dashed vertical lines mark the detection thresholds of XRT(X-ray), LSST(optical) and VLA(radio). Figure shows the sensitivity of the detection fractions on detection thresholds

Table 3. Detection thresholds of different instruments

Instrument	Frequency (Hz)	Flux threshold (mJy)
XRT	2.4×10^{18}	4.37×10^{-7}
LSST	4.5×10^{14}	5.75×10^{-4} ¹
PS1	4.5×10^{14}	5.75×10^{-3} ²
DECam	4.5×10^{14}	1.2×10^{-3} ³
JVLA	1.5×10^{10}	5.0×10^{-2}

the rates. We are also demonstrating the effect of detection sensitivity in the final rates (see next section and Figure. 2 (left)).

The detection criterion we have followed in all the bands is that a minimum of one point in the light curve should be above the threshold flux. The sensitivity of the instruments depend on the exposure time, nature of the background field, and observation conditions. The latter two factors are arbitrary and hence we are concentrating only on making sure that our detection criteria is consistent with the required exposure time. The *LSST* has a unique combination of wide field capabilities and a sensitive detector reaching up to ~ 24 mag in short exposures of 15 sec. The quoted *XRT* sensitivity requires an exposure time of 10^4 sec (ref: *XRT* website). The *JVLA* is capable of achieving $\sim 10\mu$ Jy rms in 1 hr of observations. Two adjacent points in our simulated light curves are separated such that $\delta t/t \sim 1$.

We consider 5 hours from the burst as the starting time of EM follow-up observations. This allows around 2×10^4 sec of δt . Hence, our detection criterion is consistent with the exposure time required for achieving the assumed threshold fluxes in all telescopes considered in the study. However, in Section. 4.5, we are also investigating the effect of cadence on the final rates.

4.4 Afterglow detectability

With the detection criterion described above and the instruments and thresholds shown in Table. 3, we have made detections of lightcurves in X-ray, optical and radio bands for both the populations. The quantity we are interested is the fraction of sources for which we have detectable afterglow, denoted as f_{AGdet} as described in Section. 2. In Figure. 2, we have shown features of detection fractions of different afterglow components.

The left panel in Figure. 2 shows how the detection fraction of different afterglow components grows as a function of time after the burst for a GW-detected BNS source population with 5-detector network LHVKI. The solid(dashed) curves are from SGRB population-1(2). In both the cases, it is observed that the X-ray and optical detection fractions reach the maximum in around 10 days whereas the radio detection fraction takes more than 100 days to reach the maximum. In other words, within 10 days, all the detectable afterglows are observed in X-ray and optical band whereas radio afterglows may start appearing above the threshold of the instruments several days after the burst. In almost all the observed SGRBs, X-ray and optical afterglow light curves start at the peak value and monotonically decreases with time. However, in our studies we have seen X-ray and optical afterglow fluxes reach the peak within a maximum span of 10 days. This difference is due to the fact that, our study uses the GW trigger and not the GRB prompt emission and hence our population includes outside-jet sources. All the late rising afterglow have come from outside-jet sources, whereas the observed SGRBs are all within-jet or close to it. If we consider only “within jet” sources in our simulation, all the detections happens roughly within a day.

For population-1, we detect X-rays for 23%(14.5% within-jet + 8.5% outside-jet) of the sources, optical

for 15.9%(11.3% within-jet + 4.6% outside-jet) and radio 20.6%(10.3% within-jet + 10.3% outside-jet) of the sources. 14.6% of the sources (10.2% within-jet + 4.4% outside-jet) are detected in all 3 bands whereas 73% of the sources (1% within-jet + 72% outside-jet) are not detected in any of the bands. For population-2, we detect X-rays for 36.5%(15.5% within-jet + 21% outside-jet) of the sources, optical for 35.7%(15.5% within-jet + 20.2% outside-jet) and radio 60.5%(15.5% within-jet + 4.5% outside-jet) of the sources. 34.5% of the sources (15.5% within-jet + 19% outside-jet) are detected in all 3 bands whereas 39.4% of the sources (all outside-jet) are not detected in any of the bands.

Though population-2 shows similar trends as in population-1, its detection fraction overall increases much more than population-1 in particular for radio afterglows. The overall increase in the detections can be explained as follows. Due to the uniform distribution of E_{iso} and n , 90% of the sources have $E_{iso} > 10^{51}$ and $n > 0.01$ in population-2. Whereas, in population-1, where we have uniform distributions in $\log E_{iso}$ and $\log n$, only 33% of the sources have $E_{iso} > 10^{51}$ and 33% of the sources have $n > 0.01$. This causes majority of the sources in population-2 to have relatively higher energy and denser environments resulting in an overall increase in the afterglow brightness compared to population-1, resulting in more detections. In particular, there is a large increase in radio detections compared to X-ray and optical. The synchrotron peak frequency of the power-law electron spectrum almost always crosses the radio band in the time scale of a few days for all typical ranges of physical parameters. Therefore, the radio light curve reaches the peak in a few days time, by which the jet lorentz factor drops considerably to reduce the effect of relativistic beaming. In addition to that, if there is considerable lateral spreading in the jet, the opening angle also increases by this time. This results in detections of radio afterglows even in cases where X-ray and optical are missed due to viewing angle effects. Or in other words, the highly outside-jet sources can be brought to detection in radio band especially if E_{iso} and n are high enough whereas the same can not be done for X-ray and optical. Precisely speaking, among the sources which are detected in radio but missed in X-ray and optical for population-2, $\sim 70\%$ of the sources have $\theta_v > 2\theta_j$, indicating their extremely outside-jet scenario.

It should be noted that 66%(99%) of the within-jet sources are detected in all bands whereas 85%(46%) of the outside-jet sources are not detected in any of the bands for population-1(2). This clearly indicates that the detectability is biased towards within-jet sources. To understand this further, we estimated detection fractions in all bands for within/outside jet sources separately. Among all the within-jet sources taken together, X-ray, optical and radio were detected for 94%(100%), 73%(99.9%) and 67%(99.9%) of them respectively for population-1(population-2). Conversely, among all the outside-jet sources taken together, X-ray and optical were detected only for 10%(24%) and 5%(24%) of them respectively, while radio has been detected for 12%(53%) of them for population-1(2). This means that for X-ray and optical detection, what matters is mostly sources' geometric profile (within/outside-jet nature) whereas for radio, what matters is source' intrinsic properties such as energy and number density etc. A more detailed

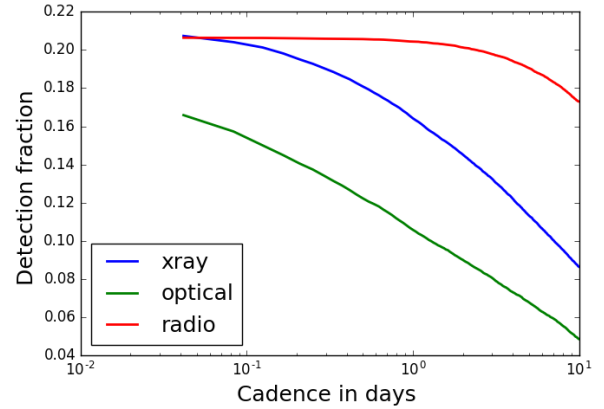


Figure 3. Detection fraction varying as a function of the cadence of the instrument (delay between the first and second observations). The x-axis of the figure shows cadence starting from 1 hour till 10 days and y-axis shows the detection fraction of the afterglow component. It can be observed that the X-ray and optical detection fractions are significantly dropped if a 1-day cadence is assumed instead of 1-hour cadence, whereas radio is unaffected by this. The reason is explained in text.

analysis will be presented in a related paper (M. Saleem 2017).

In the right panel of Figure. 2, we have shown afterglow detection fraction against the detection thresholds in mJy. The vertical lines mark the detection thresholds of *XRT*, *LSST* and *JVLA*. Figure shows that all the numbers which we compute are highly sensitive to the detection thresholds. The bumps observed for X-ray $\sim 10^{-3}$ mJy and optical around 10^{-1} mJy in population-2 are due to the within-jet population. The same results in the saturation observed in population-1 sources at high thresholds. The flux for within-jet sources are much higher compared to outside-jet sources due to beaming and hence all the within-jet population are detected even with a very shallow threshold but the bulk of the outside-jet sources can be detected only when the threshold is sufficiently deeper. As discussed before, this geometric factor is less of a factor for the radio afterglows and the radio curves are relatively smoother. The precise location of the bump depends on the ranges of the parameters, especially very strongly on θ_j , and the type of the distribution (log vs uniform). For example, we can see that due to the higher fraction of high E_{iso} and n sources, population-2 shows the difference predominantly in the form of the bump, while population-1 only shows a saturation.

4.5 Detection criterion and detectability

As we stated in Section. 4.3, we have considered one flux point above the threshold as the detection criterion. However, depending on instruments, for a confident detection, just the detection of one flux point may not often be sufficient and observations with a different criterion may affect the detection fraction too. For example, instead of one flux point, if we assume that at least two flux points are required for a confident detection, it requires that after the first observation, the telescope will have to be further scheduled for a second one with a certain time delay between them

Table 4. Rates of different afterglow components in association with the BNS mergers detected by 5-detector network LHVKI(3-detector network LHV) for population-1 and population-2 assuming a BNS merger rate of $0.6 - 774\text{Gpc}^{-3}\text{yr}^{-1}$ (and that all BNS mergers produce SGRBs). For optical detection, rates are separately quoted for current wide field instruments *Pan Starrs1* and *DECam* as well as the future wide field instrument *LSST*. The revised BNS merger rate is $320 - 4740\text{Gpc}^{-3}\text{yr}^{-1}$ (Abbott et al. 2017d). Consequently, the afterglow detection rates in the table below will also be increased (lower limits by a factor ~ 530 and upper limits by a factor ~ 6).

Afterglow observation	$R_{\text{AG,BNS}}$ with population-1 (yr^{-1})	$R_{\text{AG,BNS}}$ with population-2 (yr^{-1})
X-ray	0.04 - 53 (0.02 - 27)	0.06 - 83 (0.03 - 42)
Optical(<i>LSST</i>)	0.03 - 36 (0.01 - 19)	0.06 - 81 (0.03 - 41)
Optical(<i>PS1</i>)	0.02 - 22 (0.01 - 11)	0.04 - 57 (0.02 - 28)
Optical(<i>DECam</i>)	0.02 - 31 (0.01 - 16)	0.06 - 72 (0.03 - 36)
Radio	0.04 - 47 (0.02 - 25)	0.11 - 138 (0.05 - 69)
X-ray & optical(<i>LSST</i>)&radio	0.03 - 33 (0.01 - 18)	0.06 - 79 (0.03 - 40)
X-ray & optical(<i>PS1</i>)&radio	0.02 - 21 (0.01 - 11)	0.04 - 57 (0.02 - 28)
X-ray & optical(<i>DECam</i>)&radio	0.02 - 30 (0.01 - 16)	0.06 - 72 (0.03 - 36)
No afterglow	0.13 - 167 (0.06 - 77)	0.07 - 90 (0.03 - 39)

(known as *cadence*). Different instruments can have different *cadence*. In that case, what matters for the detectability is whether or not the afterglow flux lasts above the threshold for a duration at least equal to the delay between first and second observations. Consequently, the afterglow lightcurve whose peak flux is above the threshold are likely to be not detected if the flux does not remain above the threshold for a duration equal to the cadence of the instrument. This causes a drop down in the detection fraction. In this section, we demonstrate how our detection fractions in Section. 4.4 would have got affected if we were to consider two flux points above the threshold as the detection criterion.

Figure-3 shows the variation in detection fractions as a function of cadence. The x-axis of the figure shows cadence starting from 1 hour till 10 days and y-axis shows the fraction of lightcurves whose flux lasts above the threshold for a duration at least equal to the cadence (Note that those which lasts for a shorter duration will not be detected). It can be observed that the X-ray and optical detection fractions are significantly dropped if a 1-day cadence is assumed instead of 1-hour cadence, whereas radio is unaffected for this. This is because most of the X-ray and optical detection are from within-jet sources and which are at the peak right from the beginning of observation with a rapidly decaying profile and hence falls below the threshold immediately whereas the radio lightcurves which rises relatively later, lasts for longer duration and hence a 1-day cadence will not affect them. Moreover, a considerable fraction of radio detections comes from outside-jet sources which peaks much later and decays slowly. Due to this, detectable radio afterglows are likely to stay much longer than X-ray and optical.

5 RATES

In this section, we compute the detection rates of afterglows in association with the GW-detected BNS mergers (see Eq.1) by combining the detection fractions and detection volumes computed in previous sections (see Table. 3 and Figure. 2) with the BNS merger rates obtained from population synthesis models. We adopt the numbers obtained in Dominik et al. (2012) which estimates the BNS merger rates to be $r_{\text{BNS}} = 0.6 - 774\text{Gpc}^{-3}\text{yr}^{-1}$

With the EM facilities listed in Table. 3 and with the GW networks LHVKI and LHV, we have shown our estimates of coincident GW(BNS)-afterglow detection rates in Table. 4. Estimates with both population-1 and population-2 are shown in separate columns and numbers are quoted as their uncertainty ranges rather than mean or median. The numbers outside the bracket are the afterglow detection rates in association with the BNS merger detection by the future 5-detector network LHVKI and the numbers inside the bracket are for the existing 3-detector network LHV.

The dominant source of uncertainty in the estimates (lower-upper bounds of rates) arise from the assumptions which go into the population synthesis models whose predictions for BNS merger rate we crucially employ in our analysis. The other ingredients of rates such as detection fractions, detection volume would also have uncertainties in their estimates. GW detection fraction was estimated from a simulation which was repeated for 100 trials and found that the 1-sigma deviation is only less than 1% and hence we have not included those uncertainties. detection volume is the volume enclosing all the detections from all these 100 trials (Each trial essentially has 3×10^5 sources).

6 CAVEATS

This paper estimates the joint observation rates of GW BNS merger events and the SGRB afterglow events in the X-ray, optical and radio band. For such a scenario, we have made several assumptions which we revisit below and state possible caveats.

6.1 GW-detectability

Among the ingredients of joint detection rates in Eq.1, the GW detection fraction f_{GWdet} and detection volume V_{det} have been estimated from our simulated BNS sources, using a detection criterion of network SNR of 8. This might be an optimistic criterion compared to realistic cases where it may require to satisfy minimum SNRs at individual detectors. Using a different criterion will alter the detection fraction and detection volumes. Further, we have computed SNR using the designed sensitivity (PSD) curves of advanced LIGO.

However, in real cases, as discussed in [Nissanke et al. \(2010\)](#), the particular noise realisation of a particular source will introduce errors in the SNR and hence sub-threshold events can go above the threshold and vice versa, affecting the detection fractions slightly.

We have fixed the NS mass at $1.4M_{\odot}$. The BNS detectability can have minor variations considering the range of NS masses as $1 - 3M_{\odot}$. Further, NSBH are also plausible sources for SGRB. We did not consider this in our study.

6.2 Afterglow detectability

Another major ingredient of the joint detection rates in Eq.1 is the afterglow detection fraction f_{AGdet} which we have estimated in Section.4 and shown its features in Figure. 2. f_{AGdet} estimation is based on several assumptions. First of all, in each band, we have used specific instruments as well as detection limits as given in Table. 3. These detection limits are subject to changes for practical and observational reasons and hence to affect the estimates of f_{AGdet} .

In the current study, we have assumed that all the observations start at $t_{\text{start}} = 5$ hours since the burst (where we also assume a temporal coincidence between the SGRB burst and the BNS merger). However this is subject to the latency of GW-trigger circulation (see [Nissanke et al. \(2013\)](#) for a detailed discussion). In the current scenario, more than 5 hour latency to start EM observations is not unlikely and this can cause slight decrease in f_{AGdet} . In a future scenario where we may have automated follow-up facilities, it may be possible to start EM observation with a latency of as small as 1 hour or even earlier. We have found that if the observation starts at 1 hour instead of 5 hours, we get $\sim 10\%$ more detections in X-ray, and optical with population-1 whereas no improvement with population-2. Since radio comes later, it is mostly unaffected by the choice of t_{start} , but likely to be affected by end time t_{end} of observations. We have used $t_{\text{end}} \sim 150$ days for radio. However, radio flux can stay much longer and some of the late time radio afterglows can peak after this epoch. So, this earlier t_{end} would also have caused a slight reduction in the rate of radio afterglows. See [Feng et al. \(2014\)](#) for a detailed discussion of late time radio afterglows.

As we stated in the beginning, we have assumed sufficient EM facilities to make sure 100% follow-up to GW triggers. However, in reality, in many cases, the error regions of sky localizations provided by GW observation will be pretty large (several sq. degrees) and it will be often difficult to scan such large error regions and hence to detect the afterglows. Further, in a GW-triggered EM follow-up where the prompt emission is missed, for a large fraction of the outside-jet sources, only radio afterglows will be detectable and that too after several days. In such cases, there will be practical limitations to associate them to the GW event. Late arrival and large error regions from GW observations make it difficult to establish a temporal as well as spatial coincidence. However, such sources also have contributed to our afterglow detections and therefore we have got optimistic rate estimates.

6.3 Parameter ranges and distributions

We have estimated joint detection rates using two populations of SGRB sources (1&2). First of all, our knowledge

about the universal distribution of SGRB parameters is very limited. Unlike what we have chosen, the actual population could be a combination of population-1 and population-2 or even other populations. This could have affected our rate estimates. Now, even if we assume that population-1 (or population-2) is the universal distribution of SGRB sources, for a particular class of progenitor type (BNS in our case), the distribution of the intrinsic SGRB parameters such as E_{iso}, θ_j might be different from what we considered. For eg, θ_j for BNS progenitors may be different from those of NSBH. Or in other words, the ranges we considered for E_{iso}, θ_j etc in our study may have perhaps gone beyond the realistic ranges allowed for BNS progenitors since what we have used is ranges as inferred from observations which can have various progenitor types. [Hotokezaka et al. \(2016\)](#) has used different energy values based on progenitor types where BNS and NSBH gives different range of E_{iso} values. Such effects could have biased our rate estimates.

7 CONCLUSIONS AND FUTURE PROSPECTS

In this work, we have targeted to estimate the rate of detections of SGRB afterglows in association with the BNS merger events detected by GW detector networks. To compute rates, we have combined BNS merger rates given by population synthesis predictions in [Dominik et al. \(2012\)](#) with the detectability of GW detector networks and the afterglow detectability of EM instruments as described in Section.2.

The GW detectability (or detection fractions) is computed from a simulation of 3×10^5 BNS mergers uniformly distributed in comoving constant volume and using network SNR of 8 as the detection criterion. This gives a catalogue of BNS detection events for network configurations of 3 and 5 detectors. We noted the respective detection volume and detection fractions as given in Table. 3. To each (detected) BNS merger in this catalogue, we associated an SGRB source using D_L and θ_v (or inclination i) as parameters for the GW-EM association. Amongst the rest of the SGRB parameters, E_{iso}, n and ϵ_B are drawn from two types of distributions whose details are shown in Table. 4.2, namely population-1 and population-2. In order to assess the afterglow detectability, for all the sources in both the populations, we simulated afterglow lightcurves in X-ray, optical and radio bands using the *BoxFit* package and detection fractions are estimated using detection thresholds of specific EM instruments namely *Swift*-XRT (for X-ray), current wide field optical telescopes *Pan-STARRS1*, *DECam* and the future wide field optical telescopes LSST and the radio instrument JVLA. The details of instruments including their detection thresholds are shown in Table. 3.

The afterglow detection fraction has been shown as a function of the time after burst in Figure. 2. We have seen that within 10 days, all the detectable afterglows are observed in X-ray and optical band whereas radio afterglows may start appearing in the instruments several days after the burst. In almost all the observed SGRBs, X-ray and optical afterglow light curves start at the peak value and monotonically decreases with time. However, in our studies we have seen X-ray and optical afterglow flux reaches the peak within the maximum span of ten days. This difference is due to the

fact that our population includes outside-jet sources ($\sim 85\%$ sources of populations) and all the late rising afterglow have come from outside-jet sources, whereas the observed SGRBs are all within-jet sources. Though population-1 and population-2 shows similar trends (Figure.2), the detection fraction is higher for population-2 for all 3 bands in general, and much higher for radio in particular. This is because majority of the sources in population-2 have relatively higher energy and denser environments compared to population-1 and this results in an overall rise in the afterglow brightness and hence in the detection fractions. The large increase in radio detections is because, even highly outside-jet faint sources can be brought to detection in radio band by increasing E_{iso} and n whereas the same can not be done for X-ray and optical. This is due to the relatively lower relativistic beaming of radio emissions compared to X-ray and optical emissions. To summarise, what matters for X-ray and optical detection is mostly whether the source is within-jet or outside-jet whereas what matters for radio detection is mostly the energy and number density.

Combining above estimates, we have computed joint GW-afterglow detection rates for both population-1 and 2. The numbers have been shown in Table. 4. It is to be noted that the BNS merger rates estimated from the first two observation runs of LIGO-Virgo is several factors larger than the one which is used in this paper. The revised BNS merger rate is $320-4740 \text{ Gpc}^{-3} \text{ yr}^{-1}$ (Abbott et al. 2017d) whereas the rates used in this paper is $0.6-774 \text{ Gpc}^{-3} \text{ yr}^{-1}$ (Dominik et al. 2012). Consequently, the afterglow detection rates in Table. 4 will also be increased (lower limits by a factor ~ 530 and upper limits by a factor ~ 6). This will make the joint scenario of GW and AG detection more frequent in the advanced multi-detector era.

8 ACKNOWLEDGEMENTS

MS thanks the Max Planck Partner Group HPC facility at IISER-TVM and the HPC facility at IUCAA Pune where most of the numerical exercise is carried out. Development of the Boxfit code was supported in part by NASA through grant NNX10AF62G issued through the Astrophysics Theory Program and by the NSF through grant AST-1009863. Simulations for BOXFIT version 2 have been carried out in part on the computing facilities of the Computational Center for Particle and Astrophysics (C2PAP) of the research cooperation "Excellence Cluster Universe" in Garching, Germany. KGA is partially supported by a grant from Infosys Foundation. AP thanks the IIT-SEED grant for the research support. We would also like to thank Michael Coughlin for critical review as well as insightful inputs which helped to improve the clarity of the manuscript. This manuscript has LIGO document number P1700248.

REFERENCES

Abadie J., et al., 2010, *Classical and Quantum Gravity*, 27, 173001
 Abbott B. P., et al., 2016a, *Physical review letters*, 116, 061102
 Abbott B., et al., 2016b, *Physical Review Letters*, 116, 241103
 Abbott B. P., et al., 2017a, arXiv preprint arXiv:1706.01812
 Abbott B., et al., 2017b, arXiv preprint arXiv:1711.05578
 Abbott B. P., et al., 2017c, Submitted to: *Phys. Rev. Lett.*

Abbott B. P., et al., 2017d, *Physical Review Letters*, 119, 161101
 Abbott B., et al., 2017e, *The Astrophysical Journal Letters*, 848, L13
 Abbott B., et al., 2017f, *The Astrophysical Journal Letters*, 848, L13
 Alexander K., et al., 2017, *The Astrophysical Journal Letters*, 848, L21
 Arcavi I., et al., 2017, *Nature*, 551, nature24291
 Arun K., Tagoshi H., Pai A., Mishra C. K., 2014, *Physical Review D*, 90, 024060
 Aso Y., Michimura Y., Somiya K., Ando M., Miyakawa O., Sekiguchi T., Tatsumi D., Yamamoto H., 2013, *Phys. Rev. D*, 88, 043007
 Bartos I., Brady P., Marka S., 2013, *Class. Quant. Grav.*, 30, 123001
 Berger E., 2014, *ARA&A*, 52, 43
 Blanchet L., 2006, *Living Rev. Rel.*, 9, 4
 Blanchet L., Damour T., Iyer B. R., Will C. M., Wiseman A. G., 1995, *Phys. Rev. Lett.*, 74, 3515
 Blanchet L., Damour T., Esposito-Farèse G., Iyer B. R., 2004, *Phys. Rev. Lett.*, 93, 091101
 Clark J., Evans H., Fairhurst S., Harry I., Macdonald E., Macleod D., Sutton P., Williamson A., 2015, *The Astrophysical Journal*, 809, 53
 Coughlin M., Dietrich T., Kawaguchi K., Smartt S., Stubbs C., Ujevic M., 2017, arXiv preprint arXiv:1708.07714
 Dietrich T., Ujevic M., 2017, *Classical and Quantum Gravity*, 34, 105014
 Dominik M., Belczynski K., Fryer C., Holz D. E., Berti E., Bulik T., Mandel I., O'Shaughnessy R., 2012, *The Astrophysical Journal*, 759, 52
 Fairhurst S., 2011, *Class.Quant.Grav.*, 28, 105021
 Feng L., Vaulin R., Hewitt J., 2014, arXiv preprint arXiv:1405.6219
 Foucart F., 2012, *Physical Review D*, 86, 124007
 Ghirlanda G., et al., 2016, *Astronomy & Astrophysics*, 594, A84
 Giacomazzo B., Perna R., Rezzolla L., Troja E., Lazzati D., 2012, *The Astrophysical Journal Letters*, 762, L18
 Granot J., Guetta D., Gill R., 2017, arXiv preprint arXiv:1710.06407
 Hotokezaka K., Nissanke S., Hallinan G., Lazio T. J. W., Nakar E., Piran T., 2016, *The Astrophysical Journal*, 831, 190
 Iyer B., et al., 2011, LIGO India Technical Document, <https://dcc.ligo.org/LIGO-M1100296/public>
 Kasliwal M. M., Nissanke S., 2014, *The Astrophysical Journal Letters*, 789, L5
 Kawaguchi K., Kyutoku K., Shibata M., Tanaka M., 2016, *The Astrophysical Journal*, 825, 52
 Kim S., et al., 2017, arXiv preprint arXiv:1710.05847
 Klimenko S., et al., 2011, *Phys. Rev.*, D83, 102001
 Lazzati D., Deich A., Morsony B. J., Workman J. C., 2016, arXiv preprint arXiv:1610.01157
 M. Saleem L. Resmi K. M. A. P. K. A., 2017, arXiv preprint arXiv:1710.06102 (Submitted to MNRAS)
 Metzger B. D., Berger E., 2012, *The Astrophysical Journal*, 746, 48
 Narayan R., Paczynski B., Piran T., 1992, *Astrophys. J.*, 395, L83
 Nissanke S., Holz D. E., Hughes S. A., Dalal N., Sievers J. L., 2010, *The Astrophysical Journal*, 725, 496
 Nissanke S., Kasliwal M., Georgieva A., 2013, *The Astrophysical Journal*, 767, 124
 Pai A., Dhurandhar S., Bose S., 2001, *Phys. Rev.*, D64, 042004
 Patricelli B., Razzano M., Cella G., Fidecaro F., Pian E., Branchesi M., Stamerra A., 2016, *Journal of Cosmology and Astroparticle Physics*, 2016, 056
 Pian E., et al., 2017, *Nature*, 551, 67
 Regimbau T., Siellez K., Meacher D., Gendre B., Boër M., 2015, *The Astrophysical Journal*, 799, 69

- Salafia O. S., Colpi M., Branchesi M., Chassande-Mottin E., Ghirlanda G., Ghisellini G., Vergani S., 2017, arXiv preprint arXiv:1704.05851
- Schutz B. F., 2011, *Classical and Quantum Gravity*, **28**, 125023
- Sielles K., Boer M., Gendre B., 2013, Monthly Notices of the Royal Astronomical Society, 437, 649
- Singer L. P., et al., 2014, The Astrophysical Journal, 795, 105
- Smartt S., et al., 2017, Nature, 551, nature24303
- Tagoshi H., Mishra C. K., Pai A., Arun K., 2014, Physical Review D, 90, 024053
- Tauris T. M., et al., 2017, preprint, ([arXiv:1706.09438](#))
- Troja E., et al., 2017, Nature, 551, nature24290
- Van Eerten H., Van Der Horst A., MacFadyen A., 2012, The Astrophysical Journal, 749, 44